LETTER

https://doi.org/10.1038/s41586-019-1033-6

The unexpected surface of asteroid (101955) Bennu

D. S. Lauretta[1,12], D. N. DellaGiustina[1,12], C. A. Bennett[1], D. R. Golish[1], K. J. Becker[1], S. S. Balram-Knutson[1], O. S. Barnouin[2], T. L. Becker[1], W. F. Bottke[3], W. V. Boynton[1], H. Campins[4], B. E. Clark[5], H. C. Connolly Jr[6], C. Y. Drouet d'Aubigny[1], J. P. Dworkin[7], J. P. Emery[8], H. L. Enos[1], V. E. Hamilton[3], C. W. Hergenrother[1], E. S. Howell[1], M. R. M. Izawa[9], H. H. Kaplan[3], M. C. Nolan[1], B. Rizk[1], H. L. Roper[1], D. J. Scheeres[10], P. H. Smith[1], K. J. Walsh[3], C. W. V. Wolner[1] & The OSIRIS-REx Team[11]

NASA'S Origins, Spectral Interpretation, Resource Identification and Security-Regolith Explorer (OSIRIS-REx) spacecraft recently arrived at the near-Earth asteroid (101955) Bennu, a primitive body that represents the objects that may have brought prebiotic molecules and volatiles such as water to Earth[1]. Bennu is a low-albedo B-type asteroid[2] that has been linked to organic-rich hydrated carbonaceous chondrites[3]. Such meteorites are altered by ejection from their parent body and contaminated by atmospheric entry and terrestrial microbes. Therefore, the primary mission objective is to return a sample of Bennu to Earth that is pristine—that is, not affected by these processes[4]. The OSIRIS-REx spacecraft carries a sophisticated suite of instruments to characterize Bennu's global properties, support the selection of a sampling site and document that site at a sub-centimetre scale[5–11]. Here we consider early OSIRIS-REx observations of Bennu to understand how the asteroid's properties compare to pre-encounter expectations and to assess the prospects for sample return. The bulk composition of Bennu appears to be hydrated and volatile-rich, as expected. However, in contrast to pre-encounter modelling of Bennu's thermal inertia[12] and radar polarization ratios[13]—which indicated a generally smooth surface covered by centimetre-scale particles—resolved imaging reveals an unexpected surficial diversity. The albedo, texture, particle size and roughness are beyond the spacecraft design specifications. On the basis of our pre-encounter knowledge, we developed a sampling strategy to target 50-metre-diameter patches of loose regolith with grain sizes smaller than two centimetres[4]. We observe only a small number of apparently hazard-free regions, of the order of 5 to 20 metres in extent, the sampling of which poses a substantial challenge to mission success.

Measurements from the OSIRIS-REx spacecraft's approach to and initial survey of Bennu identified spectral features, constrained the shape, rotation period and mass, characterized the photometric properties, described the global thermal inertia and revealed the surficial characteristics of the asteroid. These data allow us to evaluate the Design Reference Asteroid (DRA), a document that we created to inform mission design on the basis of telescopic observations[14]. The DRA 'scorecard' (Table 1) tracks how our pre-encounter knowledge matches reality.

Bennu's global properties largely match those determined by the pre-encounter astronomical campaign. In disk-integrated observations, the visible-to-near-infrared spectrum has a blue (negative) slope[15], confirming the B-type taxonomy. At longer wavelengths, a 2.7-μm spectral absorption band is present, consistent with the presence of hydrated silicates. Thermal emission spectra are similar to those of CM carbonaceous chondrites and contain a spectral feature at 23 μm, which is also consistent with phyllosilicates. Thus, OSIRIS-REx spectral data support the affinity with hydrated carbonaceous chondrites indicated by ground-based observations[3].

Bennu's physical properties are also consistent with findings from the astronomical campaign (Table 1). Bennu exhibits the expected spinning-top shape[16], and its rotation period, obliquity and rotation pole are within the 1σ (σ, standard deviation) uncertainties of the ground-based values. Its shape and topography indicate low levels of internal shear strength or cohesion. A mass determination from a radio science experiment[17] yields a density of $1{,}190 \pm 13$ kg m^{-3}. The low density of Bennu is consistent with a rubble-pile structure containing 50% macroporosity, assuming a particle density characteristic of CM chondrites. Bennu thus appears to be a microgravity aggregate.

At 100 million to 1 billion years old, Bennu's surface is older than expected according to dynamical models of rubble-pile evolution, but shows overprinting from more recent activity[18]. High-standing north–south ridges extend from pole to pole[16], dominating the topography and apparently directing the flow of surface material. Recent surface processes are evident in the deficiency of small craters, infill of large craters and surface mass wasting[16,18]. Fractured boulders have morphologies that suggest the influence of impact or thermal processes.

Measurements by the OSIRIS-REx Camera Suite (OCAMS) confirm that Bennu is one of the darkest objects in the Solar System, with a global geometric albedo of 4.4%[19,20]. This finding is in agreement with pre-encounter measurements[2] and consistent with CI and CM chondrites[3].

However, Bennu's surface displays an unexpected degree of albedo heterogeneity (Fig. 1). The ratio of reflected to incident flux (I/F) of Bennu's surface at a solar phase angle of 0° (Fig. 1a) ranges from $3.3\% \pm 0.2\%$ in the dark regions (Fig. 1b) to a maximum of $\geq$15% within discrete boulders of 2–3 m (Fig. 1e). The majority of large ($\geq$30 m) boulders have an albedo similar to the global average (Fig. 1c). This wide range of albedo may confound the spacecraft guidance lidar system, requiring reassessment of the approach to sample-site targeting[4].

The darkest material is concentrated in a large outcrop in Bennu's southern ($-Z$) hemisphere (Fig. 2) and in a subset of boulders perched on the surface (Fig. 1b). Such material is also present in diffuse blanketing units that are not linked to distinct morphometric features[19]. Some instances show spectral absorption at 0.55 μm, which has not previously been reported for any dark asteroid[21]. Magnetite (Fe_3O_4) is the most likely source of this spectral feature[22]. This interpretation is consistent with the emissivity spectra obtained by the OSIRIS-REx Thermal Emission Spectrometer (OTES), which show features at 18 μm and 29 μm that may be due to magnetite[15].

The detection of magnetite on the surface of Bennu supports an affinity with both CI and some (rare) CM chondrites[23,24]. Magnetite in these meteorites is thought to be the product of aqueous alteration within a parent asteroid[25]. If so, then the darker regions of Bennu, where magnetite appears to be concentrated, may bear fresher material than the brighter regions. This interpretation is consistent with some

[1]Lunar and Planetary Laboratory, University of Arizona, Tucson, AZ, USA. [2]The Johns Hopkins University Applied Physics Laboratory, Laurel, MD, USA. [3]Southwest Research Institute, Boulder, CO, USA. [4]Department of Physics, University of Central Florida, Orlando, FL, USA. [5]Department of Physics and Astronomy, Ithaca College, Ithaca, NY, USA. [6]Department of Geology, Rowan University, Glassboro, NJ, USA. [7]NASA Goddard Space Flight Center, Greenbelt, MD, USA. [8]Department of Earth and Planetary Sciences, University of Tennessee, Knoxville, TN, USA. [9]Institute for Planetary Materials, Okayama University–Misasa, Misasa, Japan. [10]Smead Department of Aerospace Engineering, University of Colorado, Boulder, CO, USA. [11]A list of authors and their affiliations appears at the end of the paper. [12]These authors contributed equally: D. S. Lauretta, D. N. DellaGiustina. *e-mail: lauretta@orex.lpl.arizona.edu

Table 1 | The DRA scorecard: a comparison of the properties of Bennu determined from pre-encounter modelling versus OSIRIS-REx data

Property	Pre-encounter value ($\pm1\sigma$)	OSIRIS-Rex value ($\pm1\sigma$)
Size and shape		
Mean diameter (m)	492 ± 20	490.06 ± 0.16
Polar extent (m)	508 ± 52	498.49 ± 0.12
Equatorial extent (m)	$(565 \pm 10) \times (535 \pm 10)$	$(564.73 \pm 0.12) \times (536.10 \pm 0.12)$
Volume (km^3)	0.062 ± 0.006	0.0615 ± 0.0001
Surface area (km^2)	0.79 ± 0.04	0.782 ± 0.004
Mass and density		
Bulk density ($kg\ m^{-3}$)	$1{,}260 \pm 70$	$1{,}190 \pm 13$
Mass ($\times10^{10}$ kg)	7.8 ± 0.9	7.329 ± 0.009
GM ($m^3\ s^{-2}$)	5.2 ± 0.6	4.892 ± 0.006
Hill sphere radius (km)	$31.7^{+3.3}_{-4.2}$	31.05 ± 0.01
Rotational properties		
Sidereal rotation period (J200) (h)	4.296059 ± 0.000002	4.296057 ± 0.000002
Obliquity (°)	178 ± 4	177.6 ± 0.11
Pole position (RA, dec.; J2000) (°)	$+87 \pm 3, -65 \pm 3$	$+85.65 \pm 0.12, -60.17 \pm 0.09$
Rotational acceleration ($\times10^{-6}$ deg d^{-2})	2.64 ± 1.05	3.63 ± 0.52
COM/COF offset [x, y, z] (m)	Undetermined	$[1.38 \pm 0.04, -0.43 \pm 0.07, -0.12 \pm 0.27]$
Products of inertia[a] (m^2)	Undetermined	$I_{zx} = -46.70 \pm 0.05$, $I_{zy} = 11.39 \pm 0.01$
Non-principal axis rotation (°)	No evidence	$<0.2 \pm 0.2$
Surface and compositional properties		
Geometric albedo (%)	4.5 ± 0.5	4.4 ± 0.2
Normal albedo range (%)	Undetermined	3.3 to $\geq$15
Thermal inertia ($J\ m^{-2}\ s^{-0.5}\ K^{-1}$)	310 ± 70	350 ± 20
Average particle size (cm)	<1	To be determined
Largest boulder (m)	$(10–20) \pm 7.5$	Height 30 ± 3, length 58 ± 6
Number of boulders >10 m	Undetermined	208 ± 40
CSFD slope (down to 8 m)	Undetermined	-2.9 ± 0.3
Average surface slope (°)	15 ± 2.4	17 ± 2
Asteroid spectral type	B	B
Closest meteorite analogues	CI and CM chondrites	CM chondrites

Pre-encounter astronomical observations accurately characterized many of the asteroid's characteristics[1]. Most values are well within 1σ of the spacecraft-based measurements. The main area in which the pre-encounter data are inaccurate is the compositional diversity and roughness of the surface, which creates a challenge for safe collection of a representative sample. G, universal gravitational constant; M, mass; COM/COF, centre of mass/centre of figure; CSFD, cumulative size frequency distribution; RA, right ascension; dec., declination.
[a]Assuming uniform density.

studies of space weathering of carbonaceous material[26]. However, other studies that simulated micrometeorite impact-induced alteration of the Murchison CM chondrite[27] produced slight darkening and near-surface nanoparticulate sulfides and magnetite. The magnetite-bearing dark regions on Bennu therefore may consist of CM-like material that was altered during exposure to the space environment. The relationship between the duration of space exposure and albedo thus has several possible explanations.

The albedo variation on Bennu offers some insight into this relationship. Some boulders contain clasts that appear to be bound together with a darker matrix material (Fig. 1d). These clastic rocks probably formed during impacts[18], which are known to produce regolith breccias[28]. In our initial census, we see albedo variation as high as about 33% within the face of a single such boulder (Fig. 1d). This finding suggests that the relative brightness of the individual clasts is not a product of space weathering. Instead, they probably represent distinct lithologies. Elsewhere, isolated boulders occur with albedos and sizes similar to those of the clastic material[19]. These boulders may be clasts that disaggregated from breccias through mechanical weathering processes, possibly thermally induced[29]. As these rocks break down, the interclastic matrix may separate and produce fine particulate regolith. Spatially resolved global and regional spectral mapping of Bennu's surface by OSIRIS-REx will further constrain Bennu's composition, but ultimately, resolution of the questions raised by our early results relies on the successful acquisition and return of a sample. That task looks more challenging than we expected.

OTES measurements confirm the thermal inertia measured from the ground[19], which was interpreted as evidence of regolith particles[12] averaging less than 1 cm. However, high-resolution data obtained by OCAMS reveal the surface to be much rougher, with the largest boulder being 58 m across, more than 200 boulders larger than 10 m present on the surface[19] and many more boulders evident at metre scales (Table 1, Fig. 3a). This result should prompt a reassessment of the nature of asteroid surfaces as determined from thermal analysis[12,30] and from radar circular polarization ratios[13], which suggested that Bennu's surface was smooth at the scale of the shortest radar wavelength (3.5 cm) with only one boulder of 10–20 m on the surface. As the OSIRIS-REx mission collects more data, we will be able to better define the relationship between thermal inertia, regolith and boulder distribution, guiding sample-site selection and future astronomical studies of asteroids.

Bennu's shape provided additional surprises. The most prominent feature in the radar shape model[13] is a pronounced equatorial ridge. Bennu's actual equatorial ridge is muted and, even though it has a larger radius on average than the rest of the asteroid, has only isolated topographic high points[16]. This structure appears to have been substantially eroded by impacts, leaving only small residual outcrops.

The pre-encounter-predicted distribution of slopes on Bennu led us to expect a subdued topography with loose material migrating into

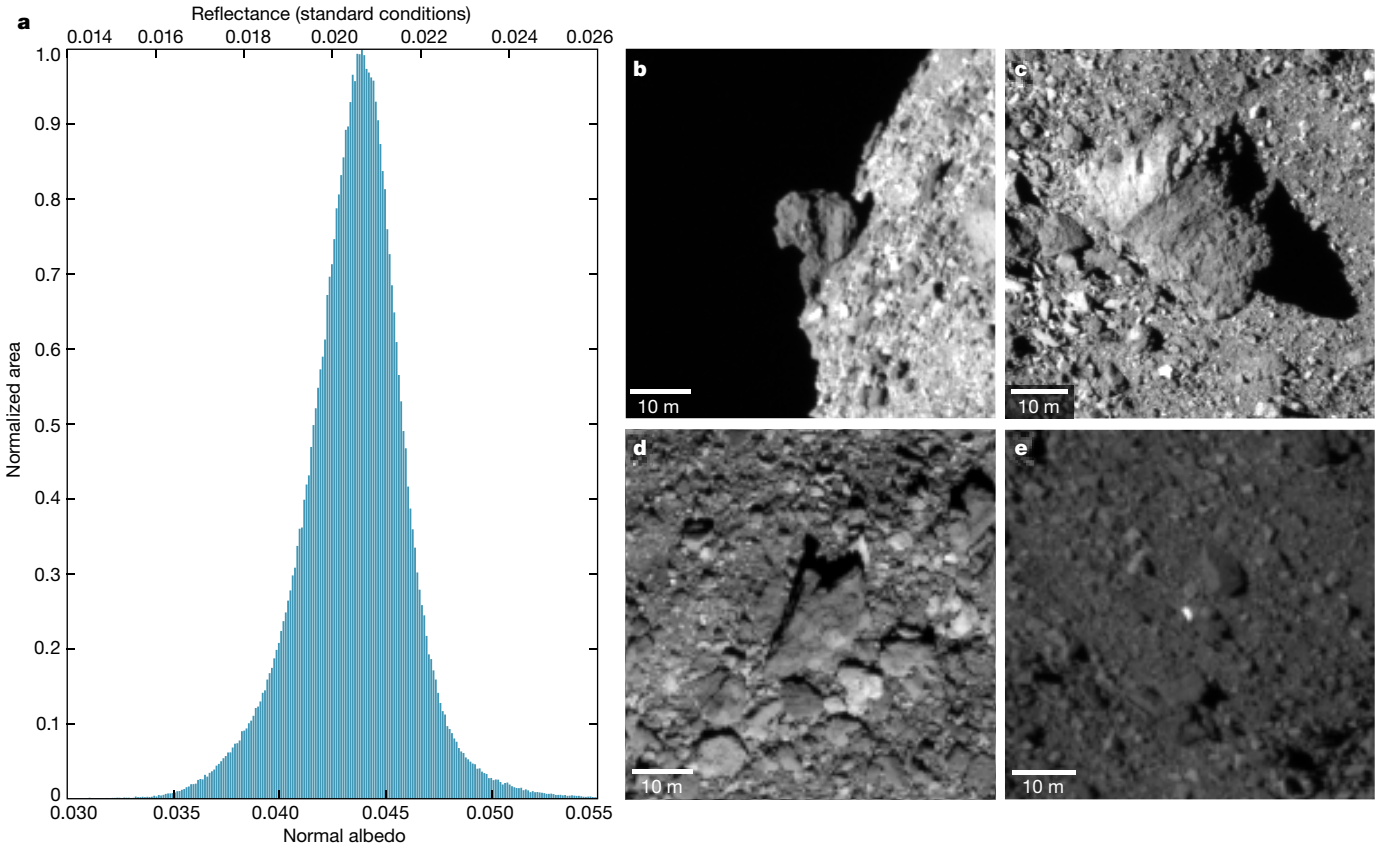

Fig. 1 | Range of albedo on the surface of Bennu. a, Histogram showing the normal albedo distribution of Bennu's surface based on low-phase-angle images acquired by the PolyCam imager[9] on 25 November 2018 (total number of pixels used as input to the histogram, 694,633). The axis along the top of the plot gives values for the same data when corrected to standard laboratory conditions (30° phase, 0° emission, 30° incidence) to enable direct comparison with the meteorite record. **b**–**e**, PolyCam images acquired on 1 and 2 December 2018 highlight the range of albedo heterogeneity on Bennu. **b**, One of the darkest boulders (about 3.3% normal albedo), perched on the surface of the asteroid (phase angle 51°, 0.32 m per pixel). **c**, A 30-m boulder that defines the prime meridian and has a near-average albedo of about 4% (phase angle 49°, 0.32 m per pixel). **d**, A boulder includes a clast that is 33% brighter than its host matrix (phase angle 33°, 0.43 m per pixel; see Methods). **e**, The brightest object identified thus far on Bennu (phase angle 34°, 0.42 m per pixel).

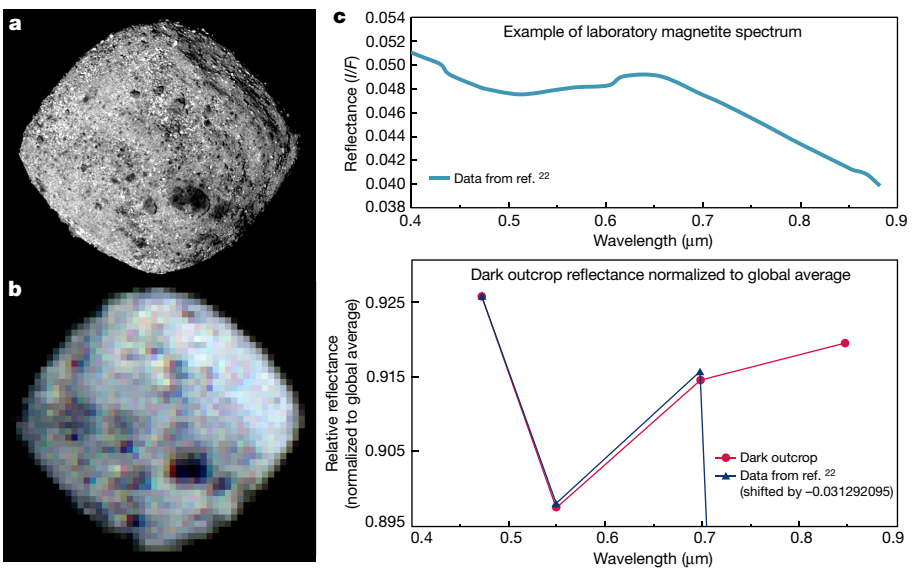

Fig. 2 | OCAMS imaging data elucidate Bennu's diverse surface reflectance and composition. a, Image acquired by the PolyCam imager on 25 November 2018 at a phase angle of about 5° and a pixel scale of about 1.1 m per pixel. **b**, Colour mosaic acquired by the MapCam imager[9] on 8 November 2018 at a phase angle of about 5° and a pixel scale of 10.9 m per pixel (coarse pixel scale is due to the wider field of view of MapCam at the larger observing distance). **c**, The upper plot shows a laboratory spectrum of magnetite[22]. The lower plot shows the laboratory magnetite spectrum in a manner comparable to the broadband spectrum from the MapCam data of 8 November 2018 for the large dark outcrop on Bennu's surface (evident in the lower centre-right of **a**, **b**). Both spectra in the lower plot are normalized to the global average reflectance of Bennu. In combination with OTES data[15], the 0.55-μm absorption feature in the MapCam data indicates the presence of magnetite on Bennu.

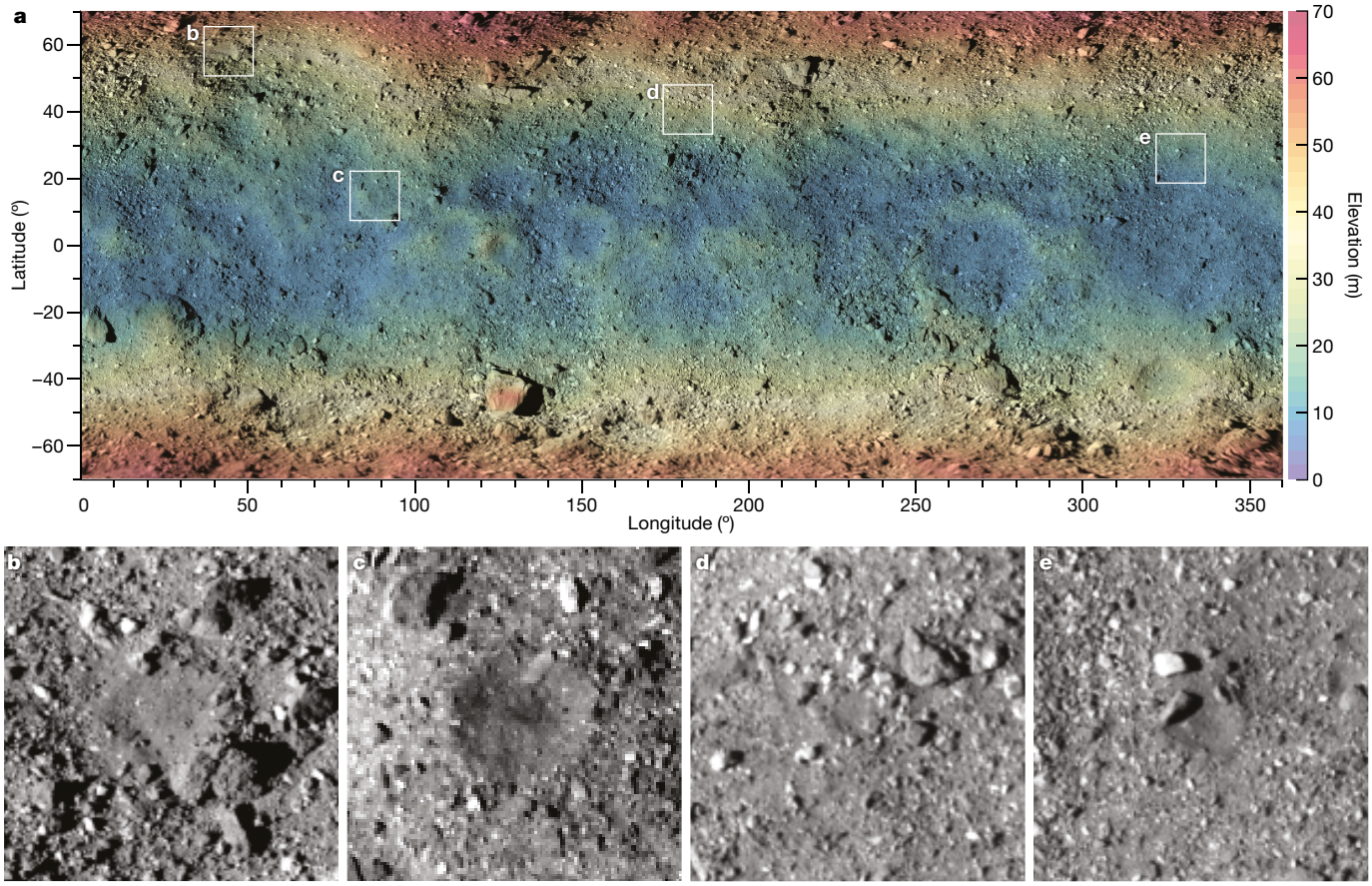

Fig. 3 | OCAMS global mosaic overlain with elevation data and four regions of interest for sampling. a, The surface of Bennu is covered by numerous boulders at the metre scale or larger. The colour scale of the overlay shows elevation above the geopotential from 0 m (blue) to 70 m (red). Vertical and horizontal axes indicate latitude and longitude, respectively. The global mosaic consists of PolyCam images taken on 1 December 2018 and MapCam images taken on 13 December 2018. White boxes corresponding to the images in **b**–**e** highlight regions of interest for sampling that appear fine-grained and relatively free of spacecraft hazards. Each of the boxes is 50 m wide, the sampling-design requirement for OSIRIS-REx navigational guidance accuracy. **b**, OCAMS image acquired on 1 December 2018 at a phase angle of 34.75° and a pixel scale of 0.42 m per pixel. **c**, OCAMS image acquired on 2 December 2018 at a phase angle of 49.25° and a pixel scale of 0.33 m per pixel. **d**, OCAMS image acquired on 2 December 2018 at a phase angle of 50.65° and a pixel scale of 0.32 m per pixel. **e**, OCAMS image acquired on 2 December 2018 at a phase angle of 48.40° and a pixel scale of 0.33 m per pixel.

geopotential lows[31]. Near-infrared spectroscopy detected a positive spectral slope corresponding to sub-Earth latitudes nearest to the equator, with the implication that this region is dominated by fine-grained material[32]. We thus hypothesized that, over time, gravel migration had built up the equatorial ridge that was apparent in the radar shape model[1]. Even though the equatorial region is the geopotential low, it is in fact dominated by large concentrations of boulders with little apparent fine-grained regolith (Fig. 3a).

Bennu does not contain the extensive patches of fine-grained regolith according to which we designed the mission[4]. However, we identified several areas, ranging from 5 to 20 m in extent, that appear relatively free of spacecraft hazards and have textures suggestive of abundant fine particles (Fig. 3). Several are associated with regions of high slope (Fig. 3b), some of these sites are at the bottom of small craters (Fig. 3c), some are ringed by metre-scale rocks (Fig. 3d) and others appear as slight depressions filled with darker fine-grained material (Fig. 3e). The high-slope regions appear promising for sample acquisition because they span the largest spatial extent.

The upcoming OSIRIS-REx site-selection campaign will provide spectroscopic and spectrophotometric measurements that will refine our understanding of Bennu's surface reflectance, mineralogical distributions, geology and thermal characteristics to complete the global assessment of the asteroid. We will select two sites, primary and backup, for detailed reconnaissance to determine whether the particles in these areas are sampleable by the spacecraft. Regardless of the final site selected, the requirements for guidance, navigation and control accuracy need to be tightened.

Bennu's unexpected nature continues to reveal itself. In January 2019, after the spacecraft's insertion into orbit around Bennu, optical navigation images detected apparent particles in the vicinity of the asteroid[20,33]. This unexpected phenomenon is under investigation. We will perform a thorough safety assessment of the asteroid environment and all potential sample sites before committing the spacecraft to descent to the surface. Although we face a reality that differs from many of our predictions, we will attempt to sample Bennu before the spacecraft departs for Earth.

Online content

Any methods, additional references, Nature Research reporting summaries, source data, statements of data availability and associated accession codes are available at https://doi.org/10.1038/s41586-019-1033-6.

Received: 25 January 2019; Accepted: 15 February 2019;
Published online 19 March 2019.

1. Lauretta, D. S. et al. The OSIRIS-REx target asteroid (101955) Bennu: constraints on its physical, geological, and dynamical nature from astronomical observations. *Meteorit. Planet. Sci.* **50**, 834–849 (2015).
2. Hergenrother, C. W. et al. Lightcurve, color and phase function photometry of the OSIRIS-REx target asteroid (101955) Bennu. *Icarus* **226**, 663–670 (2013).
3. Clark, B. E. et al. Asteroid (101955) 1999 RQ36: spectroscopy from 0.4 to 2.4 μm and meteorite analogs. *Icarus* **216**, 462–475 (2011).

4. Lauretta, D. S. et al. OSIRIS-REx: sample return from asteroid (101955) Bennu. *Space Sci. Rev.* **212**, 925–984 (2017).
5. Daly, M. G. et al. The OSIRIS-REx Laser Altimeter (OLA) investigation and instrument. *Space Sci. Rev.* **212**, 899–924 (2017).
6. Bierhaus, E. B. et al. The OSIRIS-REx spacecraft and the Touch-and-Go Sample Acquisition Mechanism (TAGSAM). *Space Sci. Rev.* **214**, 107 (2018).
7. Christensen, P. R. et al. The OSIRIS-REx thermal emission spectrometer (OTES) instrument. *Space Sci. Rev.* **214**, 87 (2018).
8. Reuter, D. C. et al. The OSIRIS-REx visible and infrared spectrometer (OVIRS): spectral maps of the asteroid Bennu. *Space Sci. Rev.* **214**, 54 (2018).
9. Rizk, B. et al. OCAMS: the OSIRIS-REx camera suite. *Space Sci. Rev.* **214**, 26 (2018).
10. Masterson, R. A. et al. Regolith X-Ray Imaging Spectrometer (REXIS) aboard the OSIRIS-REx asteroid sample return mission. *Space Sci. Rev.* **214**, 48 (2018).
11. McMahon, J. W. et al. The OSIRIS-REx radio science experiment at Bennu. *Space Sci. Rev.* **214**, 43 (2018).
12. Emery, J. P. et al. Thermal infrared observations and thermophysical characterization of OSIRIS-REx target asteroid (101955) Bennu. *Icarus* **234**, 17–35 (2014).
13. Nolan, M. C. et al. Shape model and surface properties of the OSIRIS-REx target asteroid (101955) Bennu from radar and lightcurve observations. *Icarus* **226**, 629–640 (2013).
14. Hergenrother, C. W. et al. The design reference asteroid for the OSIRIS-REx mission target (101955) Bennu. Preprint at https://arxiv.org/abs/1409.4704 (2014).
15. Hamilton, V. E. et al. Evidence for widespread hydrated minerals on asteroid (101955) Bennu. *Nat. Astron*. https://doi.org/10.1038/s41550-019-0722-2 (2019).
16. Barnouin, O. S. et al. Shape of (101955) Bennu indicative of a rubble pile with internal stiffness. *Nat. Geosci*. https://doi.org/10.1038/s41561-019-0330-x (2019).
17. Scheeres, D. J. et al. The dynamic geophysical environment of (101955) Bennu based on OSIRIS-REx measurements. *Nat. Astron*. https://doi.org/10.1038/s41550-019-0721-3 (2019).
18. Walsh, K. J. et al. Craters, boulders and regolith of (101955) Bennu indicative of an old and dynamic surface. *Nat. Geosci*. https://doi.org/10.1038/s41561-019-0326-6 (2019).
19. DellaGiustina, D. N. et al. Properties of rubble-pile asteroid (101955) Bennu from OSIRIS-REx imaging and thermal analysis. *Nat. Astron*. https://doi.org/10.1038/s41550-019-0731-1 (2019).
20. Hergenrother, C. W. et al. Operational environment and rotational acceleration of asteroid (101955) Bennu from OSIRIS-REx observations. *Nat. Commun*. https://doi.org/10.1038/s41467-019-09213-x (2019).
21. Campins, H. et al. Compositional diversity among primitive asteroids. *Prim. Meteor. Aster.* **2018**, 345–369 (2018).
22. Izawa, M. R. M. et al. Spectral reflectance properties of magnetites: implications for remote sensing. *Icarus* **319**, 525–539 (2019).
23. Kerridge, J. F., Mackay, A. L. & Boynton, W. V. Magnetite in CI carbonaceous meteorites: origin by aqueous activity on a planetesimal surface. *Science* **205**, 395–397 (1979).
24. Rubin, A. E., Trigo-Rodríguez, J. M., Huber, H. & Wasson, J. T. Progressive aqueous alteration of CM carbonaceous chondrites. *Geochim. Cosmochim. Acta* **71**, 2361–2382 (2007).
25. Brearley, A. J. in *Meteorites and the Early Solar System II* (eds Lauretta, D. S. & McSween Jr, H. Y.), 587–624 (Univ. Arizona Press, Tucson, 2006).
26. Lantz, C., Binzel, R. P. & DeMeo, F. E. Space weathering trends on carbonaceous asteroids: a possible explanation for Bennu's blue slope? *Icarus* **302**, 10–17 (2018).
27. Thompson, M. S., Loeffler, M. J., Morris, R. V., Keller, L. P. & Christoffersen, R. Spectral and chemical effects of simulated space weathering of the Murchison CM2 carbonaceous chondrite. *Icarus* **319**, 499–511 (2019).
28. Bischoff, A., Scott, E. R., Metzler, K. & Goodrich, C. A. in *Meteorites and the Early Solar System II* (eds Lauretta, D. S. & McSween Jr, H. Y.), 679–712 (Univ. Arizona Press, Tucson, 2006).
29. Delbo, M. et al. Thermal fatigue as the origin of regolith on small asteroids. *Nature* **508**, 233–236 (2014).
30. Gundlach, B. & Blum, J. A new method to determine the grain size of planetary regolith. *Icarus* **223**, 479–492 (2013).
31. Scheeres, D. J. et al. The geophysical environment of Bennu. *Icarus* **276**, 116–140 (2016).
32. Binzel, R. P. et al. Spectral slope variations for OSIRIS-REx target asteroid (101955) Bennu: possible evidence for a fine-grained regolith equatorial ridge. *Icarus* **256**, 22–29 (2015).
33. OSIRIS-REx Mission Status Update, Feb 11, 2019 https://www.asteroidmission.org/?mission_update=feb-11-2019 (2019).

Acknowledgements This material is based on work supported by NASA under contract NNM10AA11C, issued through the New Frontiers Program.

Reviewer information *Nature* thanks Harry Y. McSween Jr and the other anonymous reviewer(s) for their contribution to the peer review of this work.

Author contributions D.S.L. led the OSIRIS-REx mission, analysis and writing of the paper. D.N.D. leads the Image Processing Working Group (IPWG), which includes C.A.B., D.R.G., K.J.B., T.L.B., H.C., E.S.H. and P.H.S. The IPWG developed the image calibration pipeline, produced the global mosaic, analysed the surface for albedo variations and calculated the relative reflectance in the different MapCam filters. O.S.B. led the altimetry investigation and produced the elevation data. W.F.B. performed dynamical analysis linking Bennu to dark asteroids in the main asteroid belt. S.S.B.-K., W.V.B., B.E.C., C.Y.D.d'A., H.L.E., C.W.H., M.C.N. and B.R. designed the observation profiles and OCAMS operation plans for mission design and data acquisition. C.W.H. also led the astronomical characterization. H.C.C. Jr, J.P.D. and C.W.V.W. contributed to the content and writing of the manuscript. J.P.E. led the thermal analysis. V.E.H. led the spectral analysis, and M.R.M.I. and H.H.K. led the characterization and interpretation of the magnetite visible spectral properties. H.L.R. led the graphic design and figure development. D.J.S. led the radio science analysis and K.J.W. led the geological investigation of Bennu. The entire OSIRIS-REx Team made the encounter with Bennu possible.

Competing interests The authors declare no competing interests.

Additional information
Extended data is available for this paper at https://doi.org/10.1038/s41586-019-1033-6.
Reprints and permissions information is available at http://www.nature.com/reprints.
Publisher's note: Springer Nature remains neutral with regard to jurisdictional claims in published maps and institutional affiliations.

© The Author(s), under exclusive licence to Springer Nature Limited 2019

The OSIRIS-REx Team

D. E. Highsmith[13], J. Small[13], D. Vokrouhlický[14], N. E. Bowles[15], E. Brown[15], K. L. Donaldson Hanna[15], T. Warren[15], C. Brunet[16], R. A. Chicoine[16], S. Desjardins[16], D. Gaudreau[16], T. Haltigin[16], S. Millington-Veloza[16], A. Rubi[16], J. Aponte[17], N. Gorius[17], A. Lunsford[17], B. Allen[18], J. Grindlay[18], D. Guevel[18], D. Hoak[18], J. Hong[18], D. L. Schrader[19], J. Bayron[20], O. Golubov[21], P. Sánchez[21], J. Stromberg[22], M. Hirabayashi[23], C. M. Hartzell[24], S. Oliver[25], M. Rascon[25], A. Harch[26], J. Joseph[26], S. Squyres[26], D. Richardson[27], J. P. Emery[8], L. McGraw[8], R. Ghent[28], R. P. Binzel[29], M. M. Al Asad[30], C. L. Johnson[30,31], L. Philpott[30], H. C. M. Susorney[30], E. A. Cloutis[32], R. D. Hanna[33], H. C. Connolly Jr.[6], F. Ciceri[34], A. R. Hildebrand[34], E.-M. Ibrahim[34], L. Breitenfeld[35], T. Glotch[35], A. D. Rogers[35], B. E. Clark[5], S. Ferrone[5], C. A. Thomas[36], H. Campins[4], Y. Fernandez[4], W. Chang[37], A. Cheuvront[38], D. Trang[39], S. Tachibana[40], H. Yurimoto[40], J. R. Brucato[41], G. Poggiali[41], M. Pajola[42], E. Dotto[43], E. Mazzotta Epifani[44], M. K. Crombie[44], C. Lantz[45], M. R. M. Izawa[9], J. de Leon[46], J. Licandro[46], J. L. Rizos Garcia[46], S. Clemett[47], K. Thomas-Keprta[47], S. Van wal[48], M. Yoshikawa[48], J. Bellerose[49], S. Bhaskaran[49], C. Boyles[49], S. R. Chesley[49], C. M. Elder[49], D. Farnocchia[49], A. Harbison[49], B. Kennedy[49], A. Knight[49], N. Martinez-Vlasoff[49], N. Mastrodemos[49], T. McElrath[49], W. Owen[49], R. Park[49], B. Rush[49], L. Swanson[49], Y. Takahashi[49], D. Velez[49], K. Yetter[49], C. Thayer[50], C. Adam[51], P. Antreasian[51], J. Bauman[51], C. Bryan[51], B. Carcich[51], M. Corvin[51], J. Geeraert[51], J. Hoffman[51], J. M. Leonard[51], E. Lessac-Chenen[51], A. Levine[51], J. McAdams[51], L. McCarthy[51], D. Nelson[51], B. Page[51], J. Pelgrift[51], E. Sahr[51], K. Stakkestad[51], D. Stanbridge[51], D. Wibben[51], B. Williams[51], K. Williams[51], P. Wolff[51], P. Hayne[52], D. Kubitschek[52], M. A. Barucci[53], J. D. P. Deshapriya[53], S. Fornasier[53], M. Fulchignoni[53], P. Hasselmann[53], F. Merlin[53], A. Praet[53], E. B. Bierhaus[54], O. Billett[54], A. Boggs[54], B. Buck[54], S. Carlson-Kelly[54], J. Cerna[54], K. Chaffin[54], E. Church[54], M. Coltrin[54], J. Daly[54], A. Deguzman[54], R. Dubisher[54], D. Eckart[54], D. Ellis[54], P. Falkenstern[54], A. Fisher[54], M. E. Fisher[54], P. Fleming[54], K. Fortney[54], S. Francis[54], S. Freund[54], S. Gonzales[54], P. Haas[54], A. Hasten[54], D. Hauf[54], A. Hilbert[54], D. Howell[54], F. Jaen[54], N. Jayakody[54], M. Jenkins[54], K. Johnson[54], M. Lefevre[54], H. Ma[54], C. Mario[54], K. Martin[54], C. May[54], M. McGee[54], B. Miller[54], C. Miller[54], G. Miller[54], A. Mirfakhrai[54], E. Muhle[54], C. Norman[54], R. Olds[54], C. Parish[54], M. Ryle[54], M. Schmitzer[54], P. Sherman[54], M. Skeen[54], M. Susak[54], B. Sutter[54], Q. Tran[54], C. Welch[54], R. Witherspoon[54], J. Wood[54], J. Zareski[54], M. Arvizu-Jakubicki[1], E. Asphaug[1], E. Audi[1], R.-L. Ballouz[1], R. Bandrowski[1], K. J. Becker[1], T. L. Becker[1], S. Bendall[1], C. A. Bennett[1], H. Bloomenthal[1], D. Blum[1], W. V. Boynton[1], J. Brodbeck[1], K. N. Burke[1], M. Chojnacki[1], A. Colpo[1], J. Contreras[1], J. Cutts[1], C. Y. Drouet d'Aubigny[1], D. Dean[1], D. N. DellaGiustina[1], B. Diallo[1], D. Drinnon[1], K. Drozd[1], H. L. Enos[1], R. Enos[1], C. Fellows[1], T. Ferro[1], M. R. Fisher[1], G. Fitzgibbon[1], M. Fitzgibbon[1], J. Forelli[1], T. Forrester[1], I. Galinsky[1], R. Garcia[1], A. Gardner[1], D. R. Golish[1], N. Habib[1], D. Hamara[1], D. Hammond[1], K. Hanley[1], K. Harshman[1], C. W. Hergenrother[1], K. Herzog[1], D. Hill[1], C. Hoekenga[1], S. Hooven[1], E. S. Howell[1], E. Huettner[1], A. Janakus[1], J. Jones[1], T. R. Kareta[1], J. Kidd[1], K. Kingsbury[1], S. S. Balram-Knutson[1], L. Koelbel[1], J. Kreiner[1], D. Lambert[1], D. S. Lauretta[1], C. Lewin[1], B. Lovelace[1], M. Loveridge[1], M. Lujan[1], C. K. Maleszewski[1], R. Malhotra[1], K. Marchese[1], E. McDonough[1], N. Mogk[1], V. Morrison[1], E. Morton[1], R. Munoz[1], J. Nelson[1], M. C. Nolan[1], J. Padilla[1], R. Pennington[1], A. Polit[1], N. Ramos[1], V. Reddy[1], M. Riehl[1], B. Rizk[1], H. L. Roper[1], S. Salazar[1], S. R. Schwartz[1], S. Selznick[1], N. Shultz[1], P. H. Smith[1], S. Stewart[1], S. Sutton[1], T. Swindle[1], Y. H. Tang[1], M. Westermann[1],

C. W. V. Wolner[1], D. Worden[1], T. Zega[1], Z. Zeszut[1], A. Bjurstrom[55], L. Bloomquist[55], C. Dickinson[55], E. Keates[55], J. Liang[55], V. Nifo[55], A. Taylor[55], F. Teti[55], M. Caplinger[56], H. Bowles[57], S. Carter[57], S. Dickenshied[57], D. Doerres[57], T. Fisher[57], W. Hagee[57], J. Hill[57], M. Miner[57], D. Noss[57], N. Piacentine[57], M. Smith[57], A. Toland[57], P. Wren[57], M. Bernacki[58], D. Pino Munoz[58], S.-i. Watanabe[48,59], S. A. Sandford[60], A. Aqueche[7], B. Ashman[7], M. Barker[7], A. Bartels[7], K. Berry[7], B. Bos[7], R. Burns[7], A. Calloway[7], R. Carpenter[7], N. Castro[7], R. Cosentino[7], J. Donaldson[7], J. P. Dworkin[7], J. Elsila Cook[7], C. Emr[7], D. Everett[7], D. Fennell[7], K. Fleshman[7], D. Folta[7], D. Gallagher[7], J. Garvin[7], K. Getzandanner[7], D. Glavin[7], S. Hull[7], K. Hyde[7], H. Ido[7], A. Ingegneri[7], N. Jones[7], P. Kaotira[7], L. F. Lim[7], A. Liounis[7], C. Lorentson[7], D. Lorenz[7], J. Lyzhoft[7], E. M. Mazarico[7], R. Mink[7], W. Moore[7], M. Moreau[7], S. Mullen[7], J. Nagy[7], G. Neumann[7], J. Nuth[7], D. Poland[7], D. C. Reuter[7], L. Rhoads[7], S. Rieger[7], D. Rowlands[7], D. Sallitt[7], A. Scroggins[7], G. Shaw[7], A. A. Simon[7], J. Swenson[7], P. Vasudeva[7], M. Wasser[7], R. Zellar[7], J. Grossman[61], G. Johnston[61], M. Morris[61], J. Wendel[61], A. Burton[62], L. P. Keller[62], L. McNamara[62], S. Messenger[62], K. Nakamura-Messenger[62], A. Nguyen[62], K. Righter[62], E. Queen[63], K. Bellamy[64], K. Dill[64], S. Gardner[64], M. Giuntini[64], B. Key[64], J. Kissell[64], D. Patterson[64], D. Vaughan[64], B. Wright[64], R. W. Gaskell[31], L. Le Corre[31], J.-Y. Li[31], J. L. Molaro[31], E. E. Palmer[31], M. A. Siegler[31], P. Tricarico[31], J. R. Weirich[31], X.-D. Zou[31], T. Ireland[65], K. Tait[66], P. Bland[67], S. Anwar[68], N. Bojorquez-Murphy[68], P. R. Christensen[68], C. W. Haberle[68], G. Mehall[68], K. Rios[68], I. Franchi[69], B. Rozitis[69], C. B. Beddingfield[70], J. Marshall[70], D. N. Brack[10], A. S. French[10], J. W. McMahon[10], D. J. Scheeres[10], E. R. Jawin[71], T. J. McCoy[71], S. Russell[71], M. Killgore[72], W. F. Bottke[3], V. E. Hamilton[3], H. H. Kaplan[3], K. J. Walsh[3], J. L. Bandfield[73], B. C. Clark[73], M. Chodas[74], M. Lambert[74], R. A. Masterson[74], M. G. Daly[75], J. Freemantle[75], J. A. Seabrook[75], O. S. Barnouin[2], K. Craft[2], R. T. Daly[2], C. Ernst[2], R. C. Espiritu[2], M. Holdridge[2], M. Jones[2], A. H. Nair[2], L. Nguyen[2], J. Peachey[2], M. E. Perry[2], J. Plescia[2], J. H. Roberts[2], R. Steele[2], R. Turner[2], J. Backer[76], K. Edmundson[76], J. Mapel[76], M. Milazzo[76], S. Sides[76], C. Manzoni[77], B. May[77], M. Delbo'[78], G. Libourel[78], P. Michel[78], A. Ryan[78], F. Thuillet[78] & B. Marty[79]

[13]Aerospace Corporation, Chantilly, VA, USA. [14]Astronomical Institute, Charles University, Prague, Czech Republic. [15]Atmospheric, Oceanic and Planetary Physics, University of Oxford, Oxford, UK. [16]Canadian Space Agency, Saint-Hubert, Quebec, Canada. [17]Catholic University of America, Washington, DC, USA. [18]Center for Astrophysics, Harvard University, Cambridge, MA, USA. [19]Center for Meteorite Studies, Arizona State University, Tempe, AZ, USA. [20]City University of New York, New York, NY, USA. [21]Colorado Center for Astrodynamics Research, University of Colorado, Boulder, CO, USA. [22]Commonwealth Scientific and Industrial Research Organisation (CSIRO), Canberra, Australian Capital Territory, Australia. [23]Department of Aerospace Engineering, Auburn University, Auburn, AL, USA. [24]Department of Aerospace Engineering, University of Maryland, College Park, MD, USA. [25]Department of Astronomy and Steward Observatory, University of Arizona, Tuscon, AZ, USA. [26]Department of Astronomy, Cornell University, Ithaca, NY, USA. [27]Department of Astronomy, University of Maryland, College Park, MD, USA. [28]Department of Earth Sciences, University of Toronto, Toronto, Ontario, Canada. [29]Department of Earth, Atmospheric, and Planetary Sciences, Massachusetts Institute of Technology, Cambridge, MA, USA. [30]Department of Earth, Ocean and Atmospheric Sciences, University of British Columbia, Vancouver, British Columbia, Canada. [31]Planetary Science Institute, Tucson, AZ, USA. [32]Department of Geography, University of Winnipeg, Winnipeg, Manitoba, Canada. [33]Department of Geological Sciences, Jackson School of Geosciences, University of Texas, Austin, TX, USA. [34]Department of Geoscience, University of Calgary, Calgary, Alberta, Canada. [35]Department of Geosciences, Stony Brook University, Stony Brook, NY, USA. [36]Department of Physics and Astronomy, Northern Arizona University, Flagstaff, AZ, USA. [37]Edge Space Systems, Greenbelt, MD, USA. [38]General Dynamics C4 Systems, Denver, CO, USA. [39]Hawai'i Institute of Geophysics and Planetology, University of Hawai'i at Mānoa, Honolulu, HI, USA. [40]Hokkaido University, Sapporo, Japan. [41]INAF–Astrophysical Observatory of Arcetri, Florence, Italy. [42]INAF–Osservatorio Astronomico di Padova, Padova, Italy. [43]INAF–Osservatorio Astronomico di Roma, Rome, Italy. [44]Indigo Information Services, Tucson, AZ, USA. [45]Institut d'Astrophysique Spatiale, CNRS/Université Paris Sud, Orsay, France. [46]Instituto de Astrofísica de Canarias and Departamento de Astrofísica, Universidad de La Laguna, Tenerife, Spain. [47]Jacobs Technology, Houston, TX, USA. [48]JAXA Institute of Space and Astronautical Science, Sagamihara, Japan. [49]Jet Propulsion Laboratory, California Institute of Technology, Pasadena, CA, USA. [50]Kavli Institute for Astrophysics and Space Research, Massachusetts Institute of Technology, Cambridge, MA, USA. [51]KinetX Aerospace, Inc., Simi Valley, CA, USA. [52]Laboratory for Atmospheric and Space Physics, University of Colorado, Boulder, CO, USA. [53]LESIA, Observatoire de Paris, Université PSL, CNRS, Sorbonne Université, Univ. Paris Diderot, Sorbonne Paris Cité, Meudon, France. [54]Lockheed Martin Space, Littleton, CO, USA. [55]Macdonald, Dettwiler, and Associates, Brampton, Ontario, Canada. [56]Malin Space Science Systems, San Diego, CA, USA. [57]Mars Space Flight Facility, Arizona State University, Tempe, AZ, USA. [58]Mines ParisTech, Paris, France. [59]Nagoya University, Nagoya, Japan. [60]NASA Ames Research Center, Moffett Field, CA, USA. [61]NASA Headquarters, Washington, DC, USA. [62]NASA Johnson Space Center, Houston, TX, USA. [63]NASA Langley Research Center, Hampton, VA, USA. [64]NASA Marshall Space Flight Center, Huntsville, AL, USA. [65]Research School of Earth Sciences, Australian National University, Canberra, Australian Capital Territory, Australia. [66]Royal Ontario Museum, Toronto, Ontario, Canada. [67]School of Earth and Planetary Sciences, Curtin University, Perth, Western Australia, Australia. [68]School of Earth and Space Exploration, Arizona State University, Tempe, AZ, USA. [69]School of Physical Sciences, The Open University, Milton Keynes, UK. [70]SETI Institute, Mountain View, CA, USA. [71]Smithsonian Institution National Museum of Natural History, Washington, DC, USA. [72]Southwest Meteorite Laboratory, Payson, AZ, USA. [73]Space Science Institute, Boulder, CO, USA. [74]Space Systems Laboratory, Department of Aeronautics and Astronautics, Massachusetts Institute of Technology, Cambridge, MA, USA. [75]The Centre for Research in Earth and Space Science, York University, Toronto, Ontario, Canada. [76]U.S. Geological Survey Astrogeology Science Center, Flagstaff, AZ, USA. [77]London Stereoscopic Company, London, UK. [78]Université Côte d'Azur, Observatoire de la Côte d'Azur, CNRS, Laboratoire Lagrange, Nice, France. [79]Université de Lorraine, Nancy, France.

METHODS

The figures presented in this manuscript are derived from OCAMS observations made during the Approach and Preliminary Survey phases of the OSIRIS-REx mission[4]. The first section of Methods presents details of the image processing used to create the products in Figs. 1–3. The subsequent sections provide details on the observing profiles that were implemented to obtain the data products. The methods for determining the relationship between boulder size and normal albedo and for generating the global mosaic are included in a companion paper[19]. The data analysis methods used to obtain the parameters listed in Table 1 are provided in the other manuscripts of this package[15–20].

Image processing. *Colour images and broadband filter photometry.* We generate the OCAMS-MapCam global average spectrum shown in Fig. 2 from images acquired on 8 and 9 November 2018, with a pixel scale of about 11 m per pixel. MapCam acquired a set of colour images, one image with each filter, on each day. We register the images manually in the US Geological Survey's ISIS3 software to align the image data to their geometric backplanes. Pixels with a raw signal (measured in digital number, DN) outside the linear regime of the OCAMS detectors (1,000–14,000 DN) are scrubbed from the images. Any pixel that is scrubbed in one filter is scrubbed in all filters, so that a consistent subset of the surface is analysed in all colours. The median reflectance of the remaining pixels is calculated for each filter.

To obtain the spectrum of the dark material from the images of 8 November 2018, we combine co-registered MapCam frames into a colour cube that includes the b′, v, w and x bands. The colour cube is visualized by assigning the w, v and b′ frames into RGB colour channels. We select a 4 × 5-pixel rectangular polygon that encloses the dark spot in the RGB frame using the ISIS3 spectral plot tool. This determines the average I/F value of each band within the polygon. Values are then photometrically corrected on the basis of their observation conditions.

To compare these data with laboratory reflectance spectra of magnetite, we apply a correction to a phase angle of 30° (see section 'Reflectance distribution'). Magnetite is a common phase in aqueously altered carbonaceous chondrites. Reflectance spectra of magnetite contain a local minimum near a wavelength of 0.55 μm and a blue overall spectral slope in the range 0.4–1.0 μm. Figure 2 provides a comparison of the MapCam spectrum of Bennu's dark outcrop with the MAG105 reflectance spectrum presented in figure 7b of ref. [22], which was found to be a good match with our data. This comparison is conducted by sampling the MAG105 spectrum at the effective wavelengths of the MapCam colour bands and then shifting the spectrum linearly into the reflectance range of Bennu's surface (linearly reduced by −0.031292095, which is the difference between the reflectance of MAG105 and Bennu's dark outcrop in the b′ band). Subsequently, the spectra of Bennu's dark outcrop, as well as the resampled and reduced MAG105 sample, are divided by Bennu's global average spectrum to assess the relative reflectance of Bennu's dark outcrop and MAG105. Pure magnetite provides a qualitative spectral match to Bennu's dark material, particularly in the b, v and w bands. The x-band reflectance of the Bennu dark outcrop is higher than that of pure magnetite; however, we emphasize that the dark outcrop is unlikely to be a single phase and has an unknown grain size, therefore an exact correspondence should not be expected. Nevertheless, the MapCam multispectral data are consistent with a major contribution from magnetite, which is consistent with plausible magnetite-related features observed by OTES[15].

Reflectance distribution. We generate the reflectance (I/F) distribution shown in Fig. 1 by analysing a global mosaic of Bennu, shown in Extended Data Fig. 1. To create the mosaic, we project image data taken on 25 November 2018 with a pixel scale of about 1.2 m per pixel into a sinusoidal map projection that preserves the area, so that statistics performed on the mosaic can be interpreted as a function of area. We photometrically correct the image data to standard conditions (phase 30°, emission 0°, incidence 30°) for ease of comparison to meteorite analogues. We also calculate the normal albedo (phase 0°, emission 0°, incidence 0°), which is approximately equivalent to the geometric albedo for low-reflectance objects such as Bennu. Emission and incidence angles are corrected to the desired conditions using a Lommel–Seeliger disk function and phase angles are corrected using an exponential phase function[34]. For the correction to 0° phase angle, an additional step is performed. As the exponential phase curve used in our model does not have a term to account for the opposition surge, we perform a linear extrapolation from 2° to 0° phase angle, as these data show a change in slope that departs from the best-fit exponential function. The resulting histogram of the mosaic (Fig. 1) represents the I/F distribution across Bennu's surface as a function of surface area. Shadowed areas are removed by calculating Sun-occluded terrain using ray tracing schemes implemented in ISIS3[35] and the shape model of Bennu, and subsequently nulling those areas so that they are omitted from the final distribution.

We calculate the normal albedo variation in the brecciated rock shown in Fig. 1d by photometrically correcting the calibrated reflectance image (phase 0°, emission 0°, incidence 0°) using the photometric model developed in a companion paper[19]. We then calculate mean albedos of 0.039 and 0.053 for the areas indicated in Extended Data Fig. 2, representing the dark (blue outline) and bright (orange outline) clasts, respectively.

Approach phase observations. The Approach phase of the mission began when the OCAMS PolyCam imager optically acquired Bennu from approximately 2×10^9 km away on 17 August 2018. A schematic of the Approach timeline for the observations is given in Extended Data Fig. 3. This phase provided opportunities to view and characterize Bennu as a point source. As the range between the OSIRIS-REx spacecraft and Bennu decreased, PolyCam and MapCam collected imagery with high enough spatial resolution to derive the shape model[16], constrain the spin state[20], measure the rotational lightcurves[20], derive the phase function[20] and measure the disk-integrated spectral properties[15]. In addition to observing and characterizing Bennu itself, the Approach observations were used to search the space immediately surrounding Bennu for dust and gas plumes and natural satellites within the Hill sphere[20]. Approach data were used to follow up on ground-based observations of Bennu and to compare them to the parameters in the mission's DRA document[14].

Bennu phase function and colour imaging. Disk-integrated phase function photometry observations consisted of different activities to ensure that the phase function of Bennu was properly determined at a number of phase angles. Full-rotation phase function observations took place on two separate dates when the phase angle was between 52° and 55° and again between 20° and 50°.

These phase function observations were made on a daily basis and used optical navigation (OpNav) targeting of Bennu. The observations began on 2 October 2018 and continued through 9 November 2018. After the daily OpNav observations were complete, MapCam was used to image Bennu with the following cadence of filters: single pan image, single b′ image, single v image, single w image, single x image. The exposure times varied depending on the brightness of Bennu and were set to provide a signal-to-noise ratio of about 100. On the basis of the expected brightness of Bennu throughout Approach, the exposure times needed to be changed once per week to ensure a signal-to-noise ratio of about 100 and prevent saturation of Bennu in the images. Individual images were obtained in succession as quickly as possible to minimize photometric variations due to the rotation of Bennu. The daily images covered a phase angle range from 62° to nearly 0°.

The highest-resolution MapCam colour mosaics shown in Fig. 2 were produced using the data from the end of this observation set. MapCam imaged Bennu on 8 November 2018 at a phase angle about 5° and a pixel scale of 10.9 m per pixel.

Approach phase PolyCam imaging. Between 9 and 25 November 2018, the observational plan was to point the PolyCam nadir to Bennu and take 36 images, one at every 10° of rotation (430 s). The observation parameters are given in Extended Data Table 1. In addition to the activities noted in the table, PolyCam images taken every 10° of rotation to support the spectroscopy observations[15] were also useful in developing the shape model of Bennu[16]. These observations give a long arc of data (until 25 November 2018) over which to assess the pole direction and rotation rate[20].

Later in Approach, the field of view of PolyCam was small enough, such that we had to generate a mosaic of images to cover the area defined by the navigational uncertainties. The imaging conditions are given in Extended Data Table 2. The images were acquired with a 20% image overlap constraint and with a slew rate limit of 1.35 mrad s^{-1}. This slew rate was set by using a 10-ms exposure time and allowing for 1-pixel blurring. The area to image was covered with a raster scan consisting of long slews, with imaging and short non-imaging slews used to traverse between lines. Most of the scans accommodated navigational uncertainties at the 3σ level or greater. The images acquired on the last two days of Approach (1 and 2 December 2018) were used to generate the global mosaic shown in Fig. 3, as well as the features highlighted in Figs. 1, 3.

Preliminary Survey. The Preliminary Survey phase of the mission consisted of flybys over the north ($+Z$) pole (three flybys), equator (one flyby) and south pole (one flyby) (Extended Data Fig. 4).

Preliminary Survey MapCam observations. MapCam observations of Bennu on the 'distant' portions of the flybys were taken with a scan area sized to accommodate 2σ navigational uncertainties. To satisfy the constraint of 10° of rotational resolution, we increased the slew rate to 2.0 mrad s^{-1} from the 1.35 mrad s^{-1} value used for Approach. This higher slew rate limited the exposure time to 34 ms to avoid image blur greater than 1 pixel.

The observation parameters for all six MapCam data collection activities from the distant locations are presented in Extended Data Table 3. In addition to the size of the scans, which increase with decreasing range to the surface, the coordinates of the nadir, expressed here in the Sun anti-momentum frame, also change from the beginning to the end of the activities.

Ten dark images were planned for each MapCam activity. Five dark images with the same exposure duration as the regular images were taken before the first raster scan slew, and five additional dark images were taken following the completion of the last raster scan slew.

'Close' MapCam observations were taken on the outbound legs of the first and third north pole flybys and on the south pole flyby. The MapCam mosaics were planned around 2σ uncertainties and 20% image overlap. Ten dark images were also included, as for the 'distant' observations. The observation parameters are given in Extended Data Table 4.

High-phase-angle MapCam data for photometric models. Sets of five MapCam images, one with pan and one with each of the four colour filters, were taken at different times during Preliminary Survey. These observations span a range of phase angles from about 38° to 89°. These data contributed to achieving the accuracy and precision goals for the global MapCam photometric model data products that were necessary to build the global imaging mosaics. These data products require six photometric models: one for each MapCam filter (panchromatic, b′, v, w and x) and a PolyCam photometric model. Photometric models were used to photometrically correct global and local image mosaics. These photometrically corrected image mosaics were used as the base maps for viewing virtually all other acquired data. The MapCam colour photometric models were used to photometrically correct the global and local MapCam colour-ratio and true-colour maps.

Shape model from stereophotoclinometry. The shape model (v14)[16] was used to generate the elevation data shown in Fig. 3. Details of the stereophotoclinometry processing are given in a companion paper[16]. The shape modelling activities used data from PolyCam imaging during Approach and MapCam imaging during Preliminary Survey. From the shape model, we derived spin-state parameters and identified a prime meridian and coordinate system (used in Fig. 3). Upon encountering Bennu, a geological feature was identified and was then used as the location of Bennu's prime meridian (Fig. 1c). As higher-resolution imagery was obtained throughout the mission and the selected geological feature location became clearer, the precise location of the prime meridian was updated.

Code availability. The ISIS3 code used to generate the image processing data products is available from the US Geological Survey–Astrogeology Science Center.

Data availability

Data used in the plots in Figs. 1, 2 are available with this manuscript as Source Data. Raw and calibrated datasets will be available via the Planetary Data System (PDS) (https://sbn.psi.edu/pds/resource/orex/). Data are delivered to the PDS according to the OSIRIS-REx Data Management Plan, available in the OSIRIS-REx PDS archive. Higher-level products—for example, global mosaics and elevation maps—will be available in the Planetary Data System PDS one year after departure from the asteroid.

34. Li, J.-Y., Helfenstein, P., Buratti, B. J., Takir, D. & Clark, B. E. in *Asteroids IV* (eds Michel, P. et al.) 129–150 (Univ. Arizona Press, Tucson, 2015).
35. DellaGiustina, D. N. et al. Overcoming the challenges associated with image-based mapping of small bodies in preparation for the OSIRIS-REx mission to (101955) Bennu. *Earth Space Sci.* **5**, 929–949 (2018).

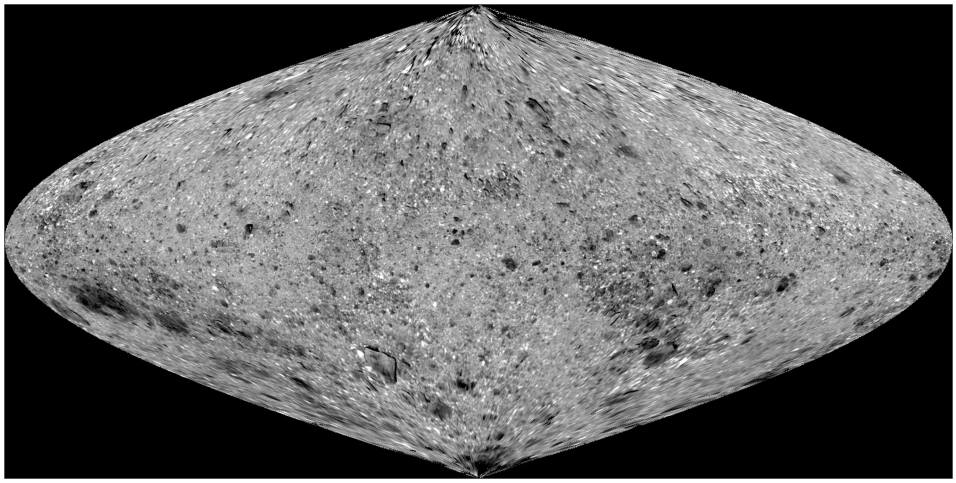

Extended Data Fig. 1 | The global mosaic of Bennu, projected onto a sinusoidal map that preserves area. The PolyCam images were photometrically corrected to mimic imaging conditions with phase, emission and incidence angles of 0°. The map has a pixel scale of 1.2 m per pixel. Images were taken on 25 November 2018.

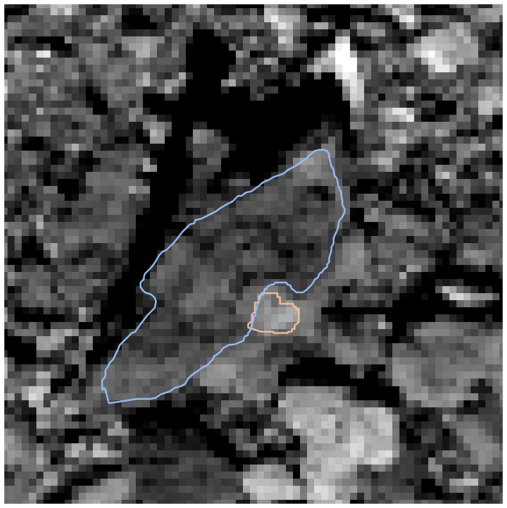

Extended Data Fig. 2 | Areas used for the calculation of the albedo variation in Fig. 1d. Blue and orange outlines represent dark and bright clasts, respectively.

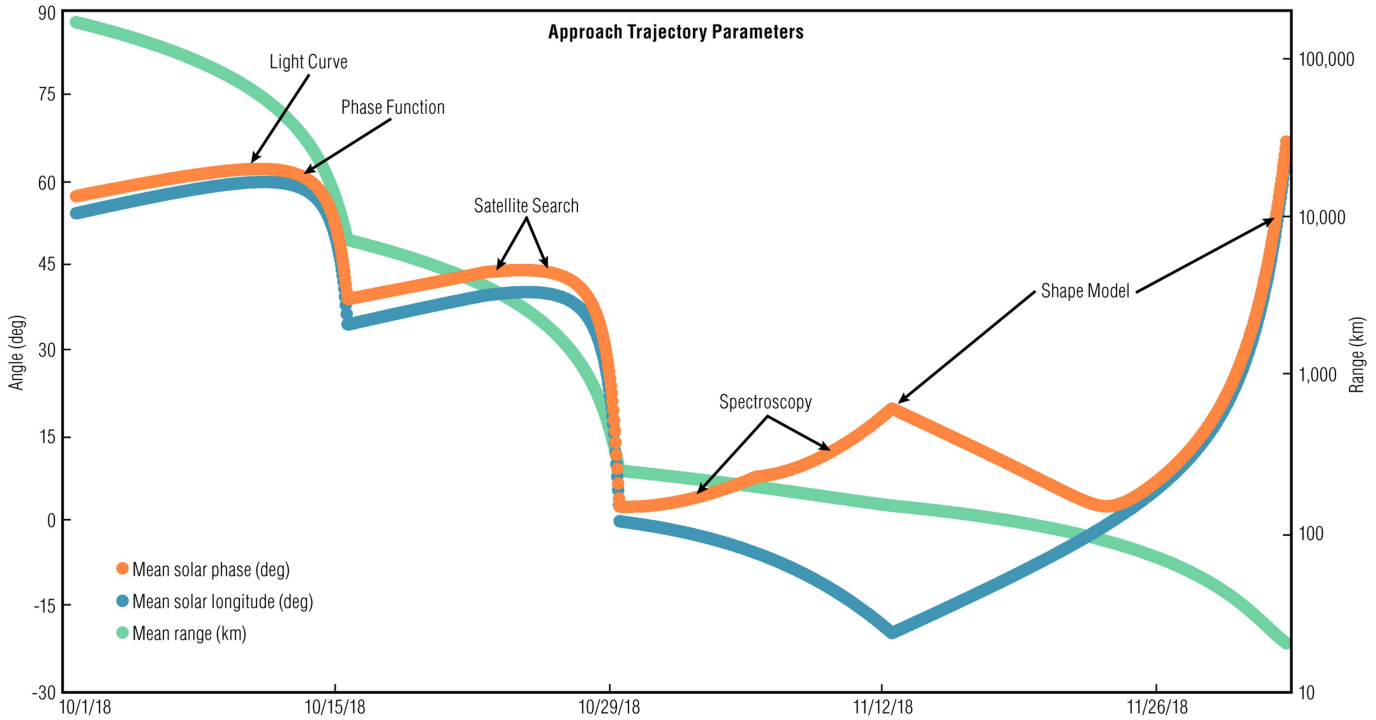

Extended Data Fig. 3 | Timeline of the various observations made during the Approach phase. The figure shows the key parameters affecting imaging conditions as a function of range to the asteroid and calendar date.

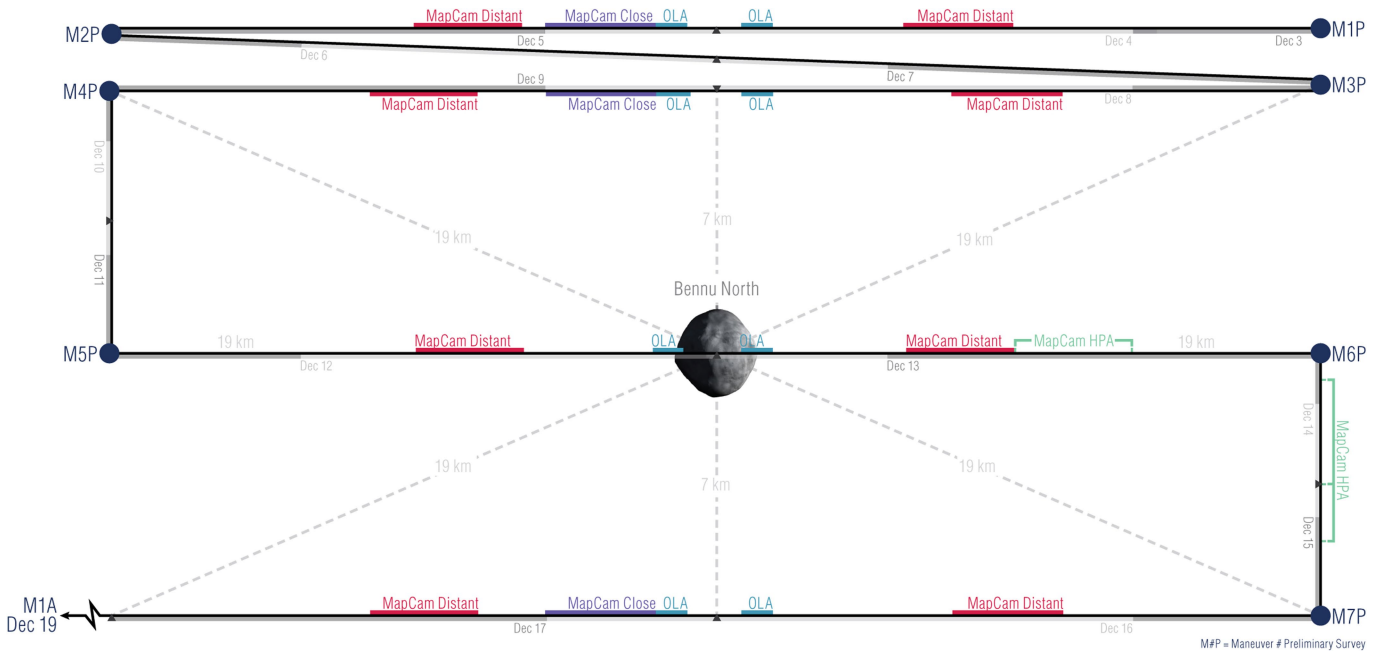

Extended Data Fig. 4 | Schematic of Preliminary Survey, showing passes over the north pole, equator, and south pole. Each trajectory leg lasts two days. The observations consist of MapCam mosaics made far from Bennu, both on the inbound and outbound legs from the closest approach, OLA observations made near the closest approach, both inbound and outbound, and additional MapCam mosaics made soon after the OLA observations but on the outbound legs of the polar flybys only. The time of closest approach to the pole was set at a nominal 17:00 UTC for all flybys.

Extended Data Table 1 | Observation parameters for early PolyCam images

Parameter	11/12/18	11/13/18	11/16/18	11/19/18	11/23/18	11/25/18
Solar Longitude (deg)	-19.1	-18.8	-13.8	-8.7	-1.1	3.4
Sigma Solar Longitude (deg)	0.4	0.3	0.3	0.4	0.7	1.0
Equivalent local time	10:43	10:44	11:04	11:25	11:55	12:13
Solar Latitude (deg)	0.0	0.1	0.6	1.2	2.4	3.3
Sigma Solar Latitude (deg)	0.4	0.3	0.4	0.5	0.8	1.1
Phase angle (deg)	19.1	18.8	13.8	8.8	2.6	4.7
Range (km)	151.8	147.4	134.9	119.7	95.0	80.6
PolyCam FOV (m)	2094	2034	1862	1652	1311	1113
PolyCam pixel size (m)	2.0	2.0	1.8	1.6	1.3	1.1
Total number of images	36	36	36	36	36	36

FOV, field of view.

Extended Data Table 2 | Observation parameters for late PolyCam images

Parameter	11/27/18	11/29/18	12/1/18	12/2/18
Solar Longitude (deg)	9.0	17.1	33.0	48.9
Sigma Solar Longitude (deg)	1.4	2.3	3.7	3.4
Equivalent local time	12:36	13:08	14:12	15:15
Sigma local time	0:05	0:09	0:14	0:13
Solar Latitude (deg)	4.7	7.2	12.4	16.8
Sigma Solar Latitude (deg)	1.6	2.4	3.2	2.4
Phase angle (deg)	10.2	18.6	35.3	51.7
Range (km)	65.0	48.4	31.2	23.8
PolyCam FOV (m)	897	668	430	328
PolyCam pixel size (m)	0.9	0.7	0.4	0.3
Number of scan lines	2	4	4	5
Number of images per line	2	4	4	6
Total number of images per mosaic	4	16	16	30
Number of mosaics	36	28	36	26
Total number of images	144	448	576	780

Extended Data Table 3 | Observation parameters for Preliminary Survey distant MapCam activities

Parameter	North Pole-1				North Pole-3				Equator				South Pole			
	Inbound (12/4)		Outbound (12/5)		Inbound (12/8)		Outbound (12/9)		Inbound (12/12)		Outbound (12/13)		Inbound (12/16)		Outbound (12/17)	
	Start	End	Start	End	Start	End	Start	End	Start	End	Start	End	Start	End	Start	End
Observation Time (UTC)	4:45	9:15	0:45	5:15	2:52	7:22	2:45	7:15	4:45	9:15	0:45	5:15	2:52	7:22	2:45	7:15
Distance to Bennu center (km)	11.4	9.1	9.1	11.4	12.4	10.0	10.0	12.5	11.1	8.8	8.8	11.1	12.5	10.0	10.1	12.6
Latitude of nadir (deg-SAM)	39.2	52.3	52.4	39.3	35.2	46.1	45.9	35.1	0.0	0.0	0.0	0.0	-35.1	-46.0	-46.0	-35.1
Longitude of nadir (deg-SAM)	89.8	89.9	-89.9	-89.8	94.4	94.5	-85.2	-85.1	-51.6	-38.2	37.9	51.4	89.7	89.8	-89.8	-89.7
Radial 1-σ uncertainty (m)	299	300	210	290	238	244	280	285	139	138	136	135	165	169	182	182
Transverse 1-σ uncertainty (m)	231	244	495	528	307	263	237	280	143	127	146	170	171	163	178	194
Normal 1-σ uncertainty (m)	369	332	241	235	253	235	239	257	187	174	159	165	230	230	238	241
Phase Angle to nadir (deg)	89.8	89.9	89.9	89.8	94.4	94.5	85.2	85.1	51.6	38.2	37.9	51.4	89.7	89.8	89.8	89.7
MapCam FOV (m)	766	612	612	766	841	673	675	842	746	590	589	746	842	675	681	849
MapCam pixel size (cm)	74.8	59.8	59.7	74.8	82.1	65.7	65.9	82.2	72.9	57.6	57.5	72.8	82.2	65.9	66.5	82.9
Mosaic Size	2x3	3x3	5x3	5x2	3x2	3x2	3x3	3x2	2x2	2x2	2x2	2x2	2x2	2x2	2x2	2x2
Rotational resolution (deg)	12		15		10		10		10		10		10		10	
Number of images per activity	267		270		216		219		144		144		144		144	

SAM, Sun anti-momentum reference frame.

Extended Data Table 4 | Observation parameters for close MapCam activities

Parameter	North Pole		North Pole		South Pole	
	12/4/18		12/8/18		12/16/18	
	Start	End	Start	End	Start	End
Observation Time (UTC)	19:30	24:00	19:30	24:00	19:30	24:00
Distance to center of Bennu (km)	7.48	8.81	7.47	8.80	7.54	8.88
Latitude of nadir (deg-SAM)	76.1	55.2	76.3	55.3	-76.4	-55.4
Radial 1-σ uncertainty (m)	201	200	284	281	186	184
Transverse 1-σ uncertainty (m)	425	488	179	211	153	167
Normal 1-σ uncertainty (m)	262	243	222	230	234	236
Phase Angle to nadir (deg)	90.0	89.9	85.3	85.2	90.0	89.9
MapCam FOV (m)	516	608	516	607	521	613
MapCam pixel size (cm)	50	59	50	59	51	60
Mosaic size	5x3	6x3	3x3	3x3	3x3	3x3
Rotational resolution (deg)	18		12		12	
Number of images per activity	327		270		270	